Progress In Electromagnetics Research, Vol. 128, 267–290, 2012

MULTILAYER MODEL FORMULATION AND ANALYSIS OF RADAR BACKSCATTERING FROM SEA ICE

M. D. Albert[1], Y. J. Lee[2, *], H. T. Ewe[2], and H. T. Chuah[2]

[1]Huawei Technologies Malaysia, Malaysia

[2]Universiti Tunku Abdul Rahman, Malaysia

Abstract—The Antarctic continent is an extremely suitable environment for the application of remote sensing technology as it is one of the harshest places on earth. Satellite images of the terrain can be properly interpreted with thorough understanding of the microwave scattering process. The proper model development for backscattering can be used to test the assumptions on the dominating scattering mechanisms. In this paper, the formulation and analysis of a multilayer model used for sea ice terrain is presented. The multilayer model is extended from the previous single layer model developed based on the Radiative Transfer theory. The Radiative Transfer theory is chosen because of its simplicity and ability to incorporate multiple scattering effects into the calculations. The propagation of energy in the medium is characterized by the extinction and phase matrices. The model also incorporates the Dense Medium Phase and Amplitude Correction Theory (DM-PACT) where it takes into account the close spacing effect among scatterers. The air-snow interface, snow-sea ice interface and sea ice-ocean interface are modelled using the Integral Equation Method (IEM). The simulated backscattering coefficients for co- and cross-polarization using the developed model for 1 GHz and 10 GHz are presented. In addition, the simulated backscattering coefficients from the multilayer model were compared with the measurement results obtained from Coordinated Eastern Artic Experiment (CEAREX) (Grenfell, 1992) and with the results obtained from the model developed by Saibun Tjuatja (based on the Matrix Doubling method) in 1992.

1. INTRODUCTION

Antarctica is the fifth largest continent in the world and plays an important role in the global climate change. In Antarctica, the extent

Received 2 February 2012, Accepted 5 May 2012, Scheduled 1 June 2012

* Corresponding author: Yu Jen Lee (leeyj@utar.edu.my).

of sea ice is about 19 million square kilometers in winter. This vast amount of sea ice cover has a critical role in balancing the world energy distribution. Constant monitoring of sea ice is needed to study the effect of global warming to the continent and other parts of the world. Monitoring the sea ice is not easy, especially when the sea ice coverage area is large. In addition, the extremeness of the climate in Antarctica is not a welcoming place for mankind.

Remote sensing technology is a good tool to use in monitoring the large sea ice area and also for data collection. Over the past 30 years, polar-orbiting satellites have revolutionized our ability to monitor the vast and data-sparse terrains. Both active and passive remote sensing satellites are used extensively for observing sea ice terrains and obtaining sea ice information such as sea ice cover extent, sea ice age, sea ice thickness and surface roughness [1]. However, the data collected through the use of satellites or radars will be meaningless without the proper understanding of the interaction and scattering mechanisms between the electromagnetic waves and the snow and sea ice.

Many forward models based on the Radiative Transfer theory had been developed to achieve this [2–6]. It is important to develop such forward models to understand various scattering mechanisms in the medium and how microwave interacts with different configuration of the medium for better interpretation of satellite images. In addition, they are also crucial towards the development of inverse models for the purpose of parameter retrieval using microwave remote sensing [7]. The traditional Radiative Transfer theory is based on the energy transport equation which was developed to treat propagation and scattering problems in the atmosphere. There are also models for sea ice that utilize the distorted Born approximation [8–12]. The advantage of this method is that it takes into account the dissipation and scattering losses and also the modification of the wave speed due to the embedded scatterers; therefore, multiple scattering has been considered to some extent.

Yet, most of these models were designed to cater for a single medium only. The terrain in the Antarctic can be more complex, for example the presence of snow cover on top of the sea ice. Therefore, a model that caters for multiple layers may be able to more accurately represent the sea ice terrain [13–15]. Besides this, the sea ice had previously been treated as a sparse medium in the models developed. The scattering from the scatterers within the medium is assumed to be independent. This assumption is not accurate since sea ice is an electrically dense medium, where the spacing between the scatterers is comparable to the wavelength [16, 17].

In this paper, a multilayer model for sea ice terrain developed based on the Radiative Transfer equation is presented. The Radiative Transfer equation is solved iteratively to include up to second order solutions so that the contributions of the major scattering mechanisms are obtained. Next, a Dense Medium Phase and Amplitude Correction Theory (DM-PACT) is included in the phase matrix of the Radiative Transfer equation to take into account the close spacing effect among the scatterers [17]. Then, the backscattering from the surfaces (air-snow interface, snow-sea ice interface and sea ice-ocean interface) is modelled using the Integral Equation Method (IEM) [18].

The effects of parameter changes such as frequency, incident angle, thickness of the layer and surface roughness of the sea ice are briefly analyzed using the developed model. In addition, a comparison between the results from the developed model and the CEAREX measurement and Matrix Doubling method is also presented.

2. MODEL CONFIGURATION & FORMULATION

2.1. Model Configuration

Figure 1 shows the cross section of sea ice terrain found in the polar region. Usually, there are 3 layers involved — the snow covering the sea ice, the sea ice itself and the ocean. The snow layer is modelled as a layer with ice particles (scatterers) embedded inside air (host medium). Meanwhile, the sea ice is modelled as a layer with bubbles or brine inclusions (scatterers) embedded inside ice (host medium).

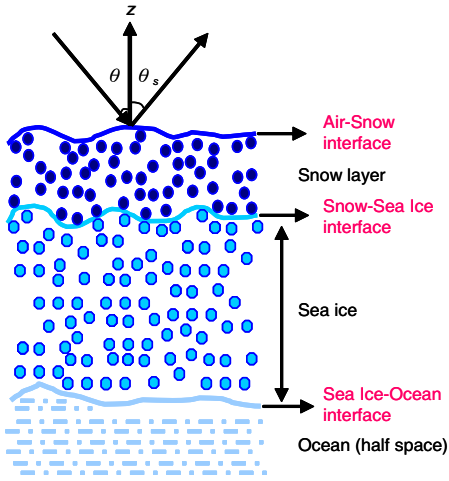

Figure 1. Model configuration of the multilayer model.

The sea ice can be divided into two types, first year sea ice and multiyear sea ice. For first year sea ice, it is found from studies that the majority of the scatterers are brine. On the other hand, multiyear sea ice scatterers are a combination of bubbles and brine inclusions.

2.2. Model Formulation

In the Radiative Transfer equation, the propagation and scattering of microwaves with a specific intensity in a medium can be written in the form of (1), where $\bar{I}$, $\bar{\bar{K}}_e$, and $\bar{\bar{P}}$ are the Stokes vector, extinction matrix and phase matrix of the medium, respectively [19]. Meanwhile $d\Omega$ and z are the solid angle and vertical direction respectively. The scattering and absorption losses of the Stokes vector along the propagation direction are taken into account by the extinction matrix. The equation is solved iteratively by including boundary conditions. The solution consists of coherent and incoherent components including surface scattering, volume scattering and surface-volume scattering for different polarizations. The detailed solution can be found in [14, 18].

$$\cos\theta \frac{d\bar{I}}{dz} = -\bar{\bar{\kappa}}_e \bar{I} + \int \bar{\bar{P}} \bar{I} d\Omega \tag{1}$$

The phase matrix used in (1) has the expression as shown in (2). $\langle|\psi|^2\rangle_n$ is the dense medium phase correction factor and $\bar{\bar{S}}$ is the Stokes' matrix for Mie scatterers with close spacing amplitude correction [20]. The dense medium phase correction factor takes into account the coherent effect of the scattering of the closely spaced scatterers. The air-snow interface, snow-sea ice interface and sea ice-ocean interface are modelled using the Integral Equation Method (IEM) [21].

$$\bar{\bar{P}}(\theta, \phi; \theta', \phi') = \langle|\psi|^2\rangle_n \cdot \bar{\bar{S}} = \begin{bmatrix} P_{vv} & P_{vh} \\ P_{hv} & P_{hh} \end{bmatrix} \tag{2}$$

In the single layer model, (1) was solved iteratively to obtain the scattering components. The advantage of this method is that the information about the scattering components from surface, surface-volume and volume interaction are known. The final result obtained, σ_{Total}, is the summation of all the scattering components, as shown in (3).

$$\sigma_{total} = \sigma_{surface} + \sigma_{volume} + \sigma_{surface\text{-}volume} \tag{3}$$

The terms of the scattering components in the multilayer model are an extension of the terms of the scattering components in the single-layer model [22, 23]. In order to develop the multilayer model, (1) was solved iteratively up to the second order. It has been found that from previous studies, the dominant scattering are usually from

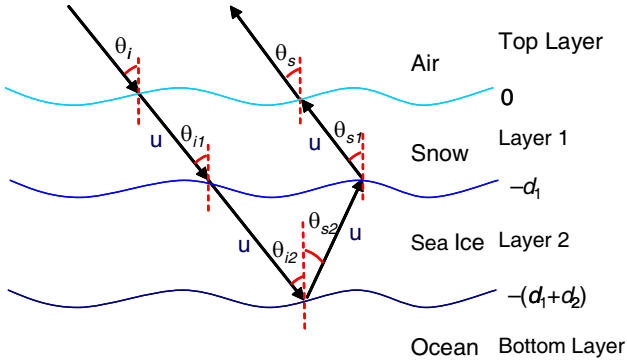

Figure 2. Cross section of the snow covered sea ice and the wave angles inside the media.

contributions up to the second order, to which subsequent orders will contribute less and less [24]. The multi-layer terms were derived for surface, volume-surface and volume scattering from both layers and boundaries. Figure 2 shows the cross section of the multi-layer and the terms used in the formulation, where d_1 and d_2 are the thicknesses for layers 1 and 2, respectively; θ_i, θ_{i1} and θ_{i2} are the incident angles at the air layer, layer 1 and layer 2 respectively. θ_s, θ_{s1} and θ_{s2} are the scattered angles at the top layer (air), layer 1 and layer 2 respectively. β denotes the incident wave polarization, α denotes the scattered wave polarization and u denotes either the horizontal or vertical polarization. The additional terms included in the multilayer model were then formulated accordingly and will be described in the following few paragraphs.

The graphical representation of all the surface backscattering components is shown in Figure 3. For this case, the additional term derived is for the surface component labeled as 1 in Figure 3. The additional backscatter coefficient term derived is (4), which shows the backscattering term of the surface backscattering from the bottom interface of layer 2. In our sea ice model, this is the interface between the sea ice and the ocean. The terms T and L in (4) denote the transmission and the lost terms, respectively. The subscripts of i and s denote the incident and scattered wave, respectively. The air-snow interface, snow-sea ice interface and sea ice-ocean interface are

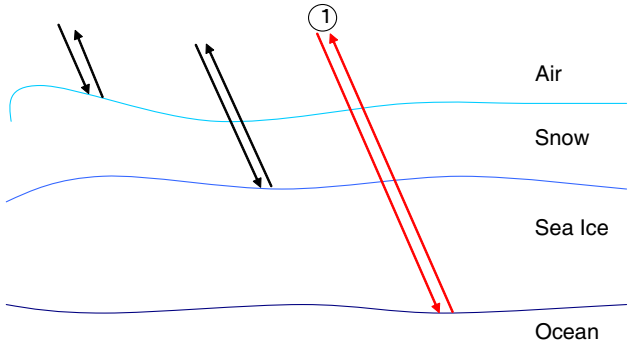

Figure 3. The backscattering coefficient terms for the surface component.

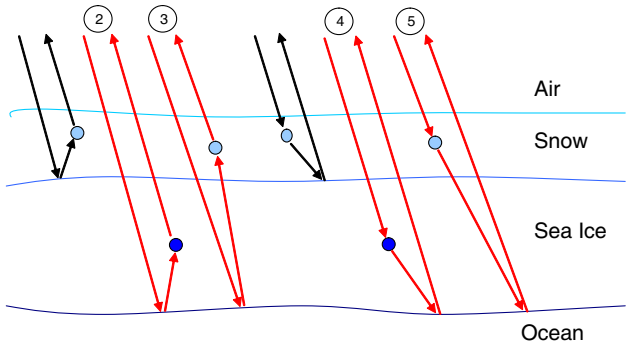

Figure 4. The backscattering coefficient terms for the surface-volume component.

modelled using IEM and the terms are labelled as σ in the equations.

$$\begin{aligned}\sigma_{\alpha\beta}^{surface} = &\cos\theta_s T_{01}(\theta_s,\theta_{s1})T_{12}(\theta_{s1},\theta_{s2})\\ &\cdot T_{21}(\pi-\theta_{i2},\pi-\theta_{i1})T_{10}(\pi-\theta_{i1};\pi-\theta_i)\\ &\cdot \sigma_{23}^{roughness}(\theta_{s2};\pi-\theta_{i2})L_{\beta1}^{-}(\theta_{i1})L_{\beta2}^{-}(\theta_{i2})L_{\alpha2}^{+}(\theta_{s2})L_{\alpha1}^{+}(\theta_{s1}) \quad (4)\end{aligned}$$

Next, the additional terms for the surface-volume component were derived. Figure 4 shows the surface-volume backscattering components and the additional terms were labelled accordingly from 2 to 5. For additional term 2, the wave is first scattered by the bottom surface of layer 2 (sea ice-ocean interface) and then scattered again upward by a scatterer in the sea ice medium. The additional term derived for this case is (5). (6) is the solution for the additional term 3, where

the incident wave is first scattered upward by the bottom surface of layer 2 before being scattered further upward by a scatterer in layer 1. Next, (7) was obtained for additional term 4, where a scatterer in layer 2 scatters the incident wave coming from layer 1 downward and the wave is then bounced back upward by the bottom surface of layer 2. Finally (8) is the derivation for the additional term 5 shown in Figure 4. In this case, the incident wave is first scattered by a scatterer in layer 1 and the wave is then bounced back from the bottom surface of layer 2 in the upward direction.

$$\begin{aligned}
&\sigma_{\alpha\beta}^{surface\text{-}volume}(\theta_s,\phi_s;\pi-\theta_i,\phi_i) \text{ for Term 2}\\
&=\frac{4\pi\cos\theta_s\times I_{\alpha\beta}^{+}(\theta_s,\phi_s;\pi-\theta_i,\phi_i)}{I_i}\\
&=\cos\theta_s\times T_{01}(\theta_s,\theta_{s1})T_{12}(\theta_{s1},\theta_{s2})\cdot T_{21}(\pi-\theta'_{i2};\pi-\theta'_{i1})T_{10}(\pi-\theta'_{i1};\pi-\theta'_{i})\\
&\quad\cdot L_{\beta1}^{-}(\theta_{i1})L_{\beta2}^{-}(\theta_{i2})L_{\alpha1}^{+}(\theta_{s1})\sec\theta_{s2}\int_0^{2\pi}\int_0^{\frac{\pi}{2}}\sin\theta'_{s2}d\theta'_{s2}d\phi'_{s2}\\
&\quad\cdot\left[\sum_{u=\alpha,\beta}P(\theta_{s2},\phi_{s2};\theta'_{s2},\phi'_{s2})\times\sigma_{u\beta}^{roughness}\right.\\
&\quad\left.\cdot(\theta'_{s2},\pi-\theta'_{i2})\left(\frac{L_{u2}^{-}(\theta'_{s2})-L_{\alpha2}^{-}(\theta_{s2})}{k_{e\alpha2}^{+}\sec\theta_{s2}-k_{eu2}^{+}\sec\theta'_{s2}}\right)\right] \qquad (5)\\
&\sigma_{\alpha\beta}^{surface-volume}(\theta_s,\phi_s;\pi-\theta_i,\phi_i) \text{ for Term 3}\\
&=\cos\theta_s T_{01}(\theta_s,\theta')T_{10}(\pi-\theta_i,\pi-\theta_{i1})\cdot T_{21}(\pi-\theta_{i2},\pi-\theta_{i1})T_{12}(\theta_{s1},\theta_{s2})\sec\theta'\\
&\quad\cdot\int_0^{2\pi}\int_0^{\frac{\pi}{2}}\sin\theta_{s2}d\theta_{s2}d\phi_{s2}\times\sigma_{u\beta}^{roughness}(\theta_{s2},\phi_{s2};\pi-\theta_{i2},\phi_{i2})\\
&\quad\cdot L_{1\beta}^{-}(\theta_{i1})L_{2\beta}^{-}(\theta_{i2})L_{2u}^{+}(\theta_{s2})\\
&\quad\cdot\sum_{u=\alpha,\beta}P(\theta',\phi';\theta_{s1},\phi_{s1})\left(\frac{L_{1u}^{+}(\theta_{s1})-L_{1\alpha}^{+}(\theta')}{k_{e\alpha}^{+}\sec\theta'-k_{eu}^{+}\sec\theta_{s1}}\right) \qquad (6)\\
&\sigma_{\alpha\beta}^{surface\text{-}volume}(\theta_s,\phi_s;\pi-\theta_i,\phi_i) \text{ for Term 4}\\
&=\cos\theta_s\times T_{01}(\theta_s,\theta_{s1})T_{12}(\theta_{s1},\theta_{s3})T_{21}(\pi-\theta_{i2},\pi-\theta_{i1})\cdot T_{10}(\pi-\theta_{i1},\pi-\theta_i)\\
&\quad\cdot L_{\alpha1}^{+}(\theta_{s1})\times I_i L_{\beta1}^{-}(\theta_{i1})L_{\alpha2}^{+}(\theta_{s3})\cdot\sec\theta_{s2}\int_0^{2\pi}\int_0^{\frac{\pi}{2}}\sin\theta'_{s2}d\theta'_{s2}d\phi'_{s2}
\end{aligned}$$

$$\cdot \left[\sum_{u=\alpha,\beta} \left(P\left(\pi-\theta_{s2},\phi_{s2};\pi-\theta'_{s2},\phi'_{s2}\right)\right) \right.$$
$$\left. \cdot\, \sigma_{u\beta}^{roughness}(\theta_{s3},\pi-\theta_{s2}) \left(\frac{L_{u2}^{-}(\theta_{s2}) - L_{\beta 2}^{-}(\theta'_{s2})}{k_{e\beta 2}^{-}\sec\theta'_{s2} - k_{eu2}^{-}\sec\theta} \right) \right] \tag{7}$$

$\sigma_{\alpha\beta}^{surface\text{-}volume}(\theta_s,\phi_s;\pi-\theta_i,\phi_i)$ for Term 5

$$= \cos\theta_s T_{01}(\theta_s,\theta_{s1}) T_{10}(\pi-\theta_i,\pi-\theta_{i1}) \cdot T_{21}(\pi-\theta_{i2},\pi-\theta') T_{12}(\theta_{s1},\theta_{s2})$$
$$\cdot\, \sec\theta' \int_0^{2\pi}\int_0^{\frac{\pi}{2}} \sin\theta_{s2} d\theta_{s2} d\phi_{s2} \times \sigma_{\alpha\beta}^{roughness}(\theta_{s2},\phi_{s2};\pi-\theta_{i2},\phi_{i2})$$
$$\cdot L_{2\beta}^{-}(\theta_{i2}) L_{2\alpha}^{+}(\theta_{s2}) L_{1\alpha}^{+}(\theta_{s1})$$
$$\cdot \sum_{u=\alpha,\beta} P(\theta',\phi';\theta_{i1},\phi_{i1}) \left(\frac{L_{1\beta}^{-}(\theta_{i1}) - L_{1u}^{-}(\theta')}{k_{eu}^{-}\sec\theta' - k_{e\beta}^{-}\sec\theta_{i1}} \right) \tag{8}$$

Lastly, Figure 5 shows the volume backscattering components and the additional terms are labelled accordingly from 6 to 10. Equations (9) to (13) show the backscattering coefficient terms for the volume components. Term 6 is the volume backscattering due to a scatterer in layer 2 (sea ice layer), where the incident wave propagates downward in layer 1 (snow layer) and is scattered in the upward direction by a scatterer in layer 2 and propagates back through layer 1. This term is given in (9).

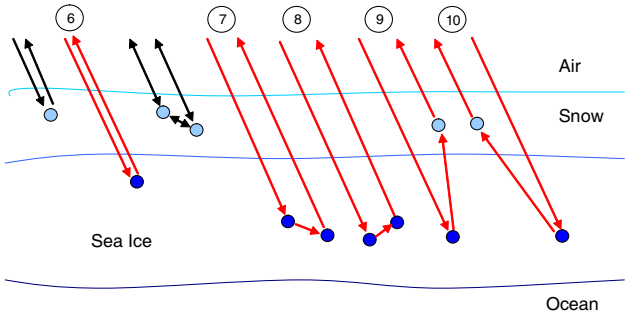

Figure 5. The backscattering coefficient terms for the surface-volume component.

$$\sigma_{\alpha\beta}^{volume}(up\text{-}down) \text{ for Term 6}$$
$$= \frac{4\pi \cos\theta_s \times I_{\alpha\beta}^{+}(\theta_s, \phi_s; \pi - \theta_i, \phi_i)}{I_i}$$
$$= 4\pi \cos\theta_s \sec\theta_{s2} T_{21}(\pi - \theta_{i2}, \pi - \theta_{i1})$$
$$\cdot T_{10}(\pi - \theta_{i1}, \pi - \theta_i) T_{12}(\theta_{s1}, \theta_{s2}) T_{01}(\theta_s, \theta_{s1})$$
$$\cdot P(\theta_{s2}, \phi_{s2}; \pi - \theta_{i2}, \phi_{i2}) \frac{1 - L_{\beta 2}^{-}(\theta'_{s2}) L_{\alpha 2}^{+}(\theta_{s2})}{k_{e\beta 2}^{-} \sec\theta'_{s2} + k_{e\alpha 2}^{+} \sec\theta_{s2}} \cdot L_{\beta 1}^{-}(\theta_{i1}) L_{1\alpha}^{+}(\theta_{s1}) \quad (9)$$

The terms 7 and 8 are given in (10) and (11), respectively. The difference between these two terms is the direction of the scattered wave by the first scatterer. In term 7, the incident wave propagates through layer 1 and is scattered by a scatterer in layer 2 in the upward direction. The wave is then scattered again by a second scatterer in layer 2 in the upward direction and propagates back through layer 1. In term 8, first scatterer in layer 2 (sea ice layer) scatters the incident wave in the downward direction and a second scatterer in the same layer then scatters the wave in the upward direction.

$$\sigma_{\alpha\beta}^{volume}(up\text{-}up\text{-}down) \text{ for Term 7}$$
$$= 4\pi \cos\theta_s T_{01}(\theta_s, \theta_{1s}) T_{\phi 0}(\pi - \theta_{i1}, \pi - \theta_{i1}) \cdot T_{21}(\pi - \theta_{i2}, \pi - \theta_{i1}) T_{12}(\theta_{s1}, \theta_{s2})$$
$$\cdot \sec\theta_{1s} \int_0^{2\pi} \int_0^{\frac{\pi}{2}} \sum_{u=\alpha,\beta} \left[\frac{\sec\theta' P_{\alpha u}(\theta_{s2}, \phi_{s2}; \theta', \phi') P_{u\beta}(\theta', \phi'; \pi - \theta_{i2}, \theta_{i2})}{K_{e\beta}^{-} \sec\theta_{i2} + K_{eu}^{+} \sec\theta'} \right.$$
$$\left. \cdot \left\{ \frac{1 - L_{\alpha}^{+}(\theta_{s2}) L_{\beta}^{-}(\theta_{i2})}{K_{e\alpha}^{+} \sec\theta_{s2} + K_{e\beta}^{-} \sec\theta_{i2}} + \frac{L_{\beta}^{-}(\theta_{i2})(L_{u}^{+}(\theta') - L_{\alpha}^{+}(\theta_{s2}))}{K_{eu}^{+} \sec\theta' - K_{e\alpha}^{+} \sec\theta_{s2}} \right\} \right]$$
$$\cdot \sin\theta' d\theta' d\phi' \times L_1^{-}(\theta_{i1}) L_1^{+}(\theta_{s1}) \quad (10)$$

$$\sigma_{\alpha\beta}^{volume}(up\text{-}down\text{-}down) \text{ for Term 8}$$
$$= 4\pi \cos\theta_s T_{01}(\theta_s, \theta_{1s}) T_{10}(\pi - \theta_{i1}, \pi - \theta_{i1}) \cdot T_{21}(\pi - \theta_{i2}, \pi - \theta_{i1}) T_{12}(\theta_{s1}, \theta_{s2})$$
$$\cdot \sec\theta_{1s} \int_0^{2\pi} \int_0^{\frac{\pi}{2}} \sum \left[\frac{\sec\theta' P_{\alpha u}(\theta_{s2}, \phi_{s2}; \pi - \theta', \phi') P_{u\beta}(\pi - \theta', \phi'; \pi - \theta_{i2}, \phi_{i2})}{K_{eu}^{-} \sec\theta' + K_{e\alpha}^{+} \sec\theta_{s2}} \right.$$
$$\left. \cdot \left\{ \frac{1 - L_{\beta}^{-}(\theta_{i2}) L_{\alpha}^{+}(\theta_{s2})}{K_{\beta}^{-} \sec\theta_{i2} + K_{\alpha}^{+} \sec\theta_{s2}} + \frac{L_{\alpha}^{+}(\theta_{s2})(L_{u}^{-}(\theta') - L_{\beta}^{-}(\theta_{i2}))}{K_{eu}^{-} \sec\theta' - K_{e\beta}^{-} \sec\theta_{i2}} \right\} \right]$$
$$\cdot \sin\theta' d\theta' d\phi' \times L_1^{-}(\theta_{i1}) L_1^{+}(\theta_{s1}) \quad (11)$$

Finally, (12) and (13) are the backscattering terms for 9 and 10 in Figure 4, respectively. In term 9, the incident wave propagates through

layer 1 and encounters the first scatterer in layer 2 and scatters upward. The wave then encounters a second scatterer in layer 1 and scatters upward again. In term 10, the wave is scattered in the downward direction by the first scatterer in layer 1 and is then scattered upward by the second scatterer in layer 2.

$$
\begin{aligned}
&\sigma^{volume}_{\alpha\beta}{}_{pq} \text{ for Term 9} \\
= \; & 4\pi \cos\theta_s T_{01}(\theta_s, \theta_{s1}) T_{10}(\pi - \theta_{i1}, \pi - \theta_{i1}) \cdot \sec\theta_{s1} T_{21}(\pi - \theta_{i2}, \pi - \theta_{i1}) \\
& \cdot \int_0^{2\pi} \int_0^{\frac{\pi}{2}} \sum_{u=1,4} \Big[\sec\theta' P_{\alpha u}(\theta_{s1}, \phi_{s1}; \theta_{s2}, \phi_{s2}) \\
& \cdot P_{u\beta}(\theta', \phi'; \pi - \theta_{i2}, \phi_{i2}) L^-_{1\beta}(\theta_{i1}) \left(\frac{L^+_{1u}(\theta') - L^+_{1\alpha}(\theta_{s1})}{k^+_{e\alpha} \sec\theta_{s1} - k^+_{eu} \sec\theta'} \right) \\
& \cdot \left(\frac{1 - L^-_{2\beta}(\theta_{i2}) L^+_{2u}(\theta')}{k^-_{e\beta} \sec\theta_{i2} + k^+_{eu} \sec\theta'} \right) \Big] \sin\theta' d\theta' d\phi' \qquad (12) \\
& \sigma^{volume}_{\alpha\beta} \text{ for Term 10} \\
= \; & 4\pi \cos\theta_s T_{01}(\theta_s, \theta_{s1}) T_{10}(\pi - \theta_{i1}, \pi - \theta_{i1}) \cdot \sec\theta_{s1} T_{12}(\theta_{s1}, \theta_{s2}) \\
& \cdot \int_0^{2\pi} \int_0^{\frac{\pi}{2}} \sum_{u=1,4} \Big[\sec\theta' P_{\alpha u}(\theta_{s2}, \phi_{s2}; \pi - \theta_{i2}, \phi) \\
& \cdot P_{u\beta}(\pi - \theta', \phi'; \pi - \theta_{i1}, \phi_{i1}) L^-_{1\alpha}(\theta_{s1}) \\
& \cdot \left(\frac{L^-_{1u}(\theta') - L^-_{1\beta}(\theta_{i1})}{k^-_{e\beta} \sec\theta_{i1} - k^-_{eu} \sec\theta'} \right) \cdot \left(\frac{1 - L^-_{2u}(\theta') L^+_{2\alpha}(\theta_{s2})}{k^-_{eu} \sec\theta' + k^+_{eu} \sec\theta_{s2}} \right) \\
& \cdot T_{21}(\pi - \theta_{i2}, \pi - \theta') \Big] \sin\theta' d\theta' d\phi' \qquad (13)
\end{aligned}
$$

3. THEORETICAL PREDICTION VALIDATION

3.1. Model Prediction Comparison with Satellites

The theoretical prediction of the backscattering coefficient using the developed model was compared with the measurements obtained from satellites. In this section, the multilayer model was used to calculate the estimated backscattering coefficient using the ground truth measurement data from randomly chosen sites that were carried out in Ross Island, Antarctica between 2002 and 2004. Images were acquired from two satellites, RADARSAT and ENVISAT as well. Both satellites are operating in the C-Band.

Figure 6 shows the location of the sites selected for the validation of the model using the RADARSAT satellite image. Sites A, B, C, I, J, K, L and P are ice shelf sites while sites D, E, F, G, H, M, N and O are sea ice sites. The parameters for selected sites used in this analysis are summarized in Appendix A. Please note that for ice shelf sites, the thickness of the ice shelf was estimated to be around 250 m as communicated with local staff in Scott Base. At this thickness, the model calculation also shows little change in backscattering returns with thicker ice shelf. Figure 7 shows the HH polarized backscattering coefficient of the model compared with the backscattering coefficient obtained from the RADARSAT image. The model seems to work rather well and gives a good prediction on the backscattering coefficients.

Next, the comparison between the backscattering coefficient obtained from the multilayer model and the one measured by ENVISAT is discussed. Unlike RADARSAT, ENVISAT has two polarization modes (VV and VH) and this enables the comparison of the backscattering coefficient for both co- and cross-polarization simultaneously. Figure 8 shows the sea ice and ice shelf sites. The sea ice sites are labelled as 1–7 while the ice shelf sites are labelled as W1–W7. Figures 9 and 10 show the comparison between the model prediction and ENVISAT for VV and VH, respectively. The parameters for selected sites used in this analysis are summarized in Appendix B. For both VV and VH polarizations, the backscattering coefficient prediction of the model showed is comparable with the backscattering data obtained from ENVISAT.

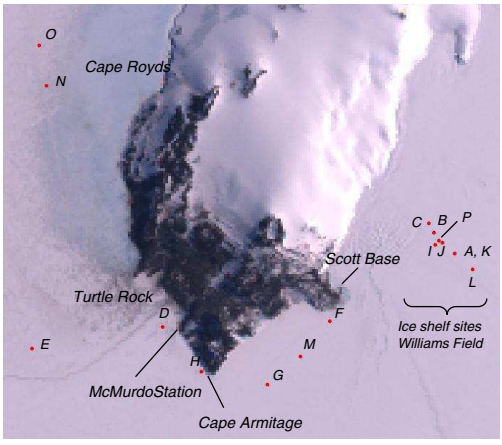

Figure 6. Sea ice and ice shelf sites (A-P).

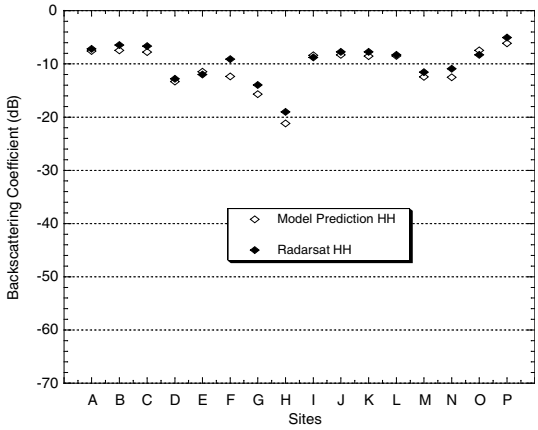

Figure 7. *HH* polarized backscattering coefficient of model prediction and RADARSAT for A-P sites.

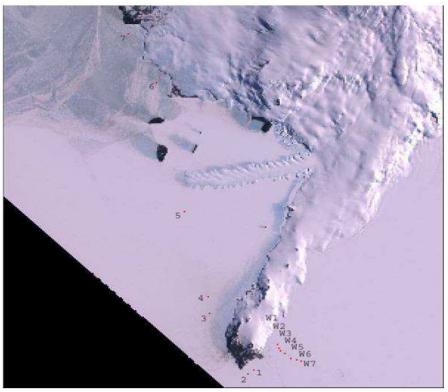

Figure 8. Sea ice and ice shelf sites labeled (1–7, W1–W7).

3.2. Comparison between Different Models

The backscattering coefficient from the multilayer model was also compared with the CEAREX measurements and the model developed by Saibun Tjuatja based on the Matrix Doubling method in 1992. During the winters of 1988 and 1989, the backscattering and emission measurements were performed on multiyear sea ice, for the Coordinated Eastern Artic Experiment (CEAREX) [25]. The two sites chosen for comparison were DS-7 and DS-9. Next, a multilayer model based on Matrix Doubling was developed by Saibun Tjuatja in 1992 [26]. The model was applied to inhomogeneous media such as

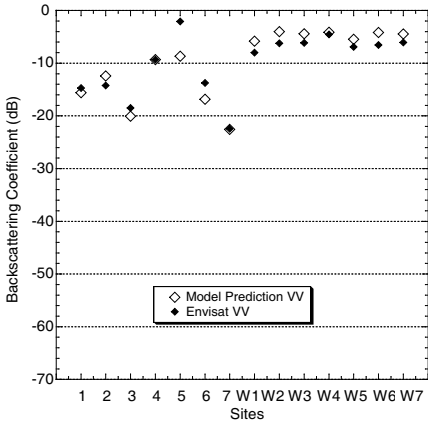

Figure 9. VV polarized backscattering coefficient of model prediction and ENVISAT.

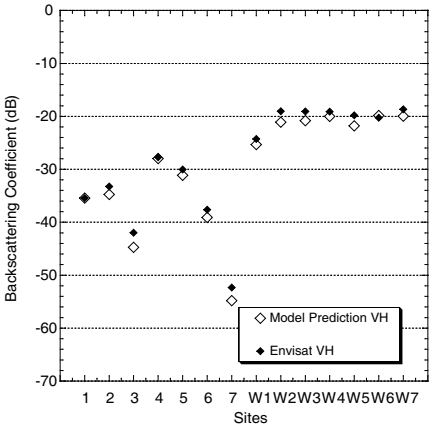

Figure 10. VH polarized backscattering coefficient of model prediction and ENVISAT.

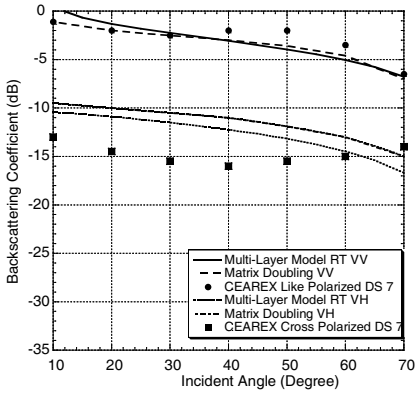

Figure 11. Backscattering coefficient (VV and VH polarizations) against incident angle for site DS-7 for 10 GHz.

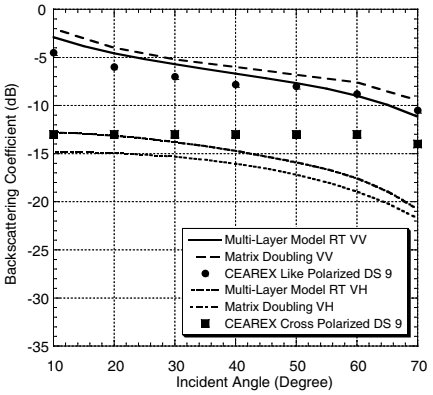

Figure 12. Backscattering coefficient (VV and VH polarizations) against incident angle for site DS-9 for 10 GHz.

snow and sea ice. Further details regarding the model can be found in [18, 27]. Saibun (1992) also performed the comparison study between the backscattering from their model and the backscattering from the CEAREX measurements.

The results of the comparison for sites DS-7 and DS-9 are shown in Figures 11 and 12, respectively. The parameters used in this analysis

are summarized in [25, 27]. The figures show that the backscattering coefficient from multilayer model using Radiative Transfer Theory agrees well with the multilayer model using the Matrix Doubling model. It was observed also that both models are comparable with the CEAREX measurements in the case of the co-polarization than in the case of cross-polarization.

4. THEORETICAL ANALYSIS

In this section, a theoretical analysis using the multilayer model was done by varying a single parameter input in the model while keeping the other parameters constant. From the simulations, the backscattering coefficient trend was studied. This study provided us with useful information on the sensitivity of backscattering coefficient when certain parameters were varied in model. The sensitivity study also gave a clearer picture on the important parameters that influenced the backscattering coefficient value. For this analysis, some typical parameter values measured in the field work or found in the literature were used (for snow, sea ice and ocean). The parameters used in this analysis are summarized in Appendix C.

4.1. Sea Ice Thickness

In this simulation, the breakdown of the backscattering coefficients for the major backscattering components is analyzed for different sea ice thicknesses at 1 GHz for co-polarized wave. This is shown in Figure 13. This is followed by Figure 14, which presents the backscattering coefficient for surface components at different sea ice thicknesses at 1 GHz for co-polarized wave.

The surface backscattering interface that contributes mainly to the total surface backscattering is at sea ice-ocean interface. The backscattering coefficient from sea ice-ocean surface interface is the highest for all sea ice thicknesses. There are two reasons for the sea ice-ocean surface interface to be the dominant factor in the total surface backscattering. One is the wave penetration ability and second is the relative permittivity difference between the layers. Penetration depth of wave is inversely proportional to the frequency of the wave. This relationship is explained further in Figure 14.

At 1 GHz the ability of the wave to penetrate through the snow layer and the sea ice layer is high. Therefore, the wave could easily reach the bottom of the sea ice. Sea ice with smaller thickness permits more waves to go through it with less attenuation. This explains the reason of high backscattering coefficient for the smaller sea ice

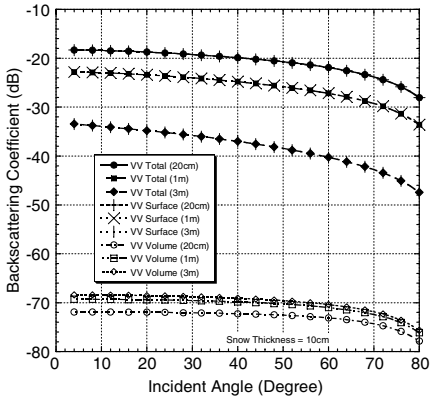

Figure 13. Backscattering coefficient for major backscattering components (VV polarization) against incident angle for various sea ice thicknesses at 1 GHz frequency.

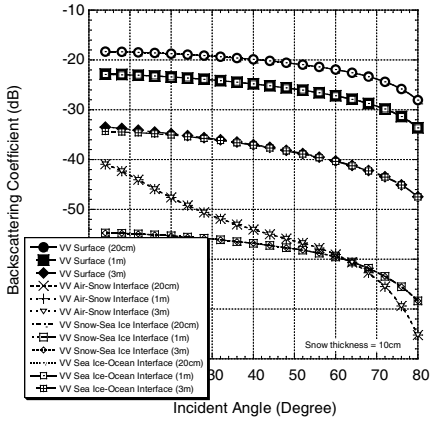

Figure 14. Backscattering coefficient for surface backscattering components (VV polarization) against incident angle for various sea ice thicknesses at 1 GHz frequency.

thicknesses. The trend of backscattering for the HH polarization is similar to VV polarization, and therefore it is not shown here. The cross polarization wave is also not shown here as the backscattering for this polarization at 1 GHz is very low.

4.2. Snow Thickness

Snow is also an important parameter that influences the backscattering coefficients. The detailed surface backscattering components are plotted in Figure 15. The plot shows that the majority of surface backscattering comes from the sea ice-ocean interface. At 1 GHz, the penetration depth of the wave in the snow and sea ice layers is high. Therefore, the wave that reaches the sea ice-ocean interface is then backscattered by the interface as there is large difference in the relative permittivity between sea ice and ocean. It is interesting to see from the plot that the snow thickness does not affect much the total surface backscattering in the co-polarized wave at 1 GHz. This information is important to be taken into account during the snow thickness retrieval process.

Cross-polarization backscattering is important to be considered when the total backscattering is dominated by the volume backscattering. Wave with high frequency such as 10 GHz interacts with the

scatterers more and scatterers in all direction. In this case, it is expected to see more cross-polarization scattered in the backscattered direction. The cross-polarization can be useful, as theoretically the more the wave interacts with the scatterers the more the cross-polarized wave is backscattered.

Figure 16 shows the volume backscattering components in detail where volume backscattering component is mainly contributed by the volume backscattering in the snow layer. At high frequencies such as 10 GHz, the wave is backscattered mostly by the scatterers in the snow layer itself where the contribution of volume backscattering in the sea ice layer is relatively small. The total backscattering for cross-polarization is influenced by the volume backscattering in the snow medium. As there is some relationship between the thickness of snow layer and the volume backscattering from the snow layer, it is possible that the cross-polarization value at high frequency (e.g., 10 GHz) be utilized to predict the thickness of the snow. However other parameters involved in the simulation have collective effects on the backscattering coefficient, therefore more testing and verification could give us better evidence in utilizing this approach to predict snow thickness.

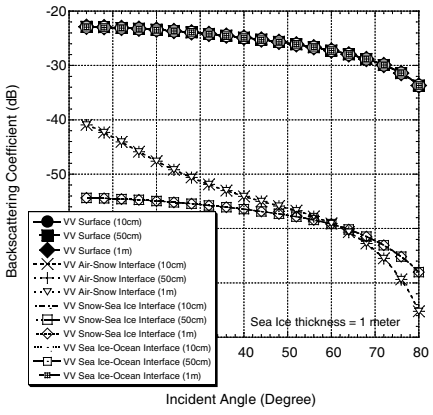

Figure 15. Backscattering coefficient for surface backscattering components (VV polarization) against incident angle for various snow thicknesses at 1 GHz frequency.

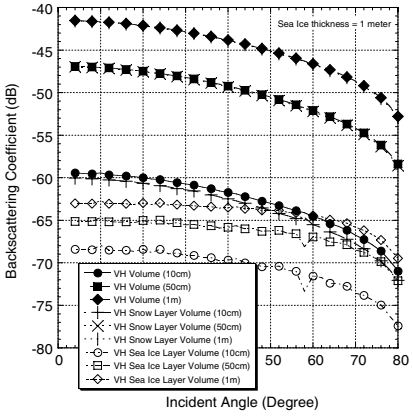

Figure 16. Backscattering coefficient for volume backscattering components (VH polarization) against incident angle for various snow thicknesses at 10 GHz frequency.

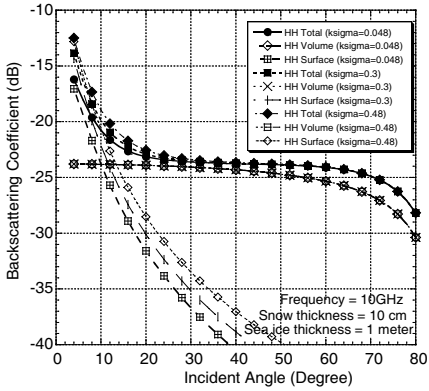

Figure 17. Backscattering coefficient for major backscattering components (HH polarization) against incident angle for various $k\sigma$ of air-snow interface at 10 GHz frequency.

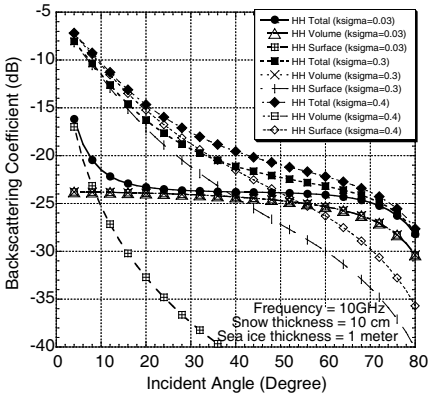

Figure 18. Backscattering coefficient for major backscattering components (HH polarization) against incident angle for various $k\sigma$ of snow-sea ice interface at 10 GHz frequency.

4.3. Surface Roughness of Snow and Sea Ice

In the next set of simulations, the surface roughness parameter will be varied and its influence to the backscattering coefficient is studied. Roughness of a surface can be described with its standard deviation of the surface height variation (RMS height) and surface correlation length (l) [28]. In this simulation kl is fixed and $k\sigma$ is varied (k is given as $2\pi/\lambda$). The $k\sigma$ values used in the simulation are 0.048, 0.3 and 0.48 respectively. The ratio of σ/l indicates the roughness of a surface. Rougher surface gives a high ratio and vice versa. This study is important as due to strong wind and changing wind direction in Antarctica, the change of snow surface roughness can be quite frequent. Firstly the effect of variation of surface roughness at air-snow interface will be studied and later this is continued with surface roughness variation at snow-sea ice interface.

Figure 17 shows the major backscattering components for various $k\sigma$ of air-snow surface interface for HH polarization respectively. The cross-polarization plots are not shown as the backscattering coefficient is small. It can be seen that the surface backscattering component is important at low incidence angle and is higher for higher $k\sigma$.

Next, the effects of $k\sigma$ variation of the snow-sea ice interface to the backscattering coefficient are discussed. The $k\sigma$ is varied and kl is fixed for this simulation. Figure 18 shows the major backscattering

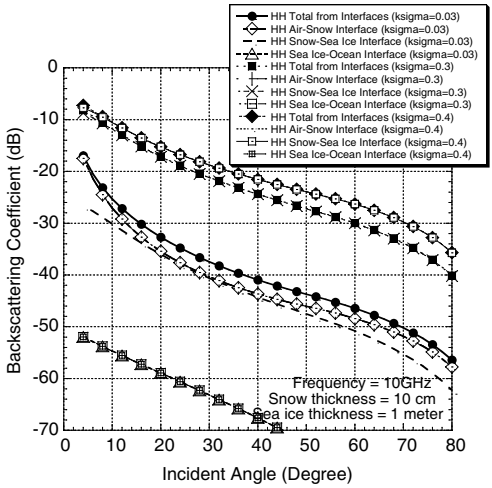

Figure 19. Backscattering coefficient for surface backscattering components (HH polarization) against incident angle for various $k\sigma$ of snow-sea ice interface at 10 GHz frequency.

components of HH polarization. Figure 19 reveals that the higher $k\sigma$ results in higher backscattering coefficient. There is an increase in the angular range (in dominance for surface backscattering) as the $k\sigma$ increases. The reason for this can be explained by referring to Figure 17. From this plot, it is found that the variation in $k\sigma$ of snow-sea ice interface is proportional to the total surface backscattering. Thus, as the $k\sigma$ increases the snow-sea ice interface is rougher. Rougher surface contributes to high incoherent scattering. As a result, the increase in this incoherent scattering contributes and increases the backscattering.

5. SUMMARY AND CONCLUSION

In this paper, a multilayer theoretical model for electrically dense media based on the Radiative Transfer Theory has been developed. The model provides a general understanding of the scattering mechanisms inside the sea ice medium and caters well for sea ice terrain with snow cover. The advantage of solving the Radiative Transfer equation iteratively is that the backscattering component information is preserved. This information is vital for researchers who work in the remote sensing area, especially sea ice terrain. In the first part of the paper, the results of the backscattering coefficient

predictions using the model are presented. Results show that the multilayer model is able to provide a way to predict the backscattering coefficient using input parameters from the field measurements at Ross Island, Antarctica. In addition, a comparison between the performance of the multilayer model and other models was carried out. The comparisons show that the multilayer model can give an equally good result with information about scattering mechanisms involved. In the second part of the paper, simulations were done to show that the backscattering coefficient depends on the physical parameters of the sea ice. Utilizing the model, simulations were carried out to better understand the interaction between microwaves and sea ice. The effect of physical parameters such as snow, sea ice thickness and surface roughness to the backscattering is studied. It can be seen that, different physical parameters affect the backscattering coefficient at different degrees. In summary, the penetration depth of microwave is inversely proportional to the frequency of the wave between the range of frequencies considered. High frequency waves (10 GHz) give more volume backscattering contribution compared to surface or surface-volume backscattering component. At low frequency (1 GHz), surface backscattering is the dominant component. The majority of co-polarized backscattering comes from surface backscattering component, while cross polarized backscattering comes from volume backscattering component. Rougher surface interface contributes to high incoherent scattering thus increasing the total backscattering coefficient.

APPENDIX A. TABLE 1: PARAMETERS DETAILS FOR SEA ICE AND ICE SHELF SITES (2002–2004)

	Sea Ice Sites 2002–2004					
	Parameters	Site D		Site E	Site F	
Snow layer	Layer thickness (m)	0.6		0.49	0.4	
	Volume fraction of scatterer (%)	32*				
	Scatterer radius (mm)	1.1+				
	Relative permittivity of top layer	1.0 , 0.0				
	Relative permittivity of scatterer	1.61E+00	7.25E−05	1.37E+00	4.10E−05	1.37E+00	4.10E−05
	Background relative permittivity	1.0 , 0.0				

Snow layer	Relative permittivity of bottom layer	Effective permittivity of bottom layer (sea ice)					
	Top surface RMS and correlation length (cm)	5.19	5.30	10.02	3.55	4.69	5.43
	Bottom surface RMS and correlation length(cm)	4.71	5.83	1.94	3.02	2.44	3.29
Sea Ice layer	Layer thickness (m)	2.63		3.22		2.35	
	Volume fraction of scatterer (%)	2*					
	Scatterer radius (mm)	0.56+					
	Relative permittivity of top layer	Effective permittivity of top layer (snow)					
	Relative permittivity of scatterer	1.0 , 0.0					
	Background relative permittivity	3.16E+00	3.43E−02	3.16E+00	5.88E−02	3.25E+00	4.11E−01
	Relative permittivity of bottom layer	5.86E+01	4.67E+00	5.86E+01	4.16E+01	5.86E+01	4.16E+01
	Top surface RMS and correlation length	Same as bottom surface RMS and Correlation length of snow layer					
	Bottom surface RMS and correlation length (cm)	0.028 , 2.1+					

* and + denote averaged value and estimated value respectively

	Ice Shelf Sites 2002 – 2004						
	Parameters	Site A		Site B		Site C	
	Volume fraction of scatterer (%)	32*					
	Scatterer radius (mm)	1.1+					
	Relative permittivity of top layer	1.0 , 0.0					
	Relative permittivity of scatterer	1.58E+00	7.39E−05	1.50E+00	6.72E−05	1.58E+00	7.39E−05
	Background relative permittivity	1.0 , 0.0					
	Relative permittivity of bottom layer	59.00 , 42.00*					
	Top surface RMS and correlation length (cm)	0.39	2.10	0.51	3.17	0.39	2.10

* and + denote averaged value and estimated value respectively

APPENDIX B. TABLE 2: PARAMETERS DETAILS FOR SEA ICE AND ICE SHELF SITES (2005)

	Sea Ice Sites 2005					
	Parameters	Site 1		Site 2		
Snow layer	Layer thickness (m)	0.96		1.11		
	Volume fraction of scatterer (%)	32*				
	Scatterer radius (mm)	1.1+				
	Relative permittivity of top layer	1.0 , 0.0*				
	Relative permittivity of scatterer	1.71E+00	8.64E −05	1.67E+00	8.07E −05	
	Background relative permittivity	1.0 , 0.0*				
	Relative permittivity of bottom layer	Effective permittivity of bottom layer (sea ice)				
	Top surface RMS and correlation length (cm)	1.35	10.95	0.60	7.54	
	Bottom surface RMS and correlation length(cm)	0.73	2.05	6.00	13.21	
Sea Ice layer	Layer thickness (m)	3.00		2.20		
	Volume fraction of scatterer (%)	2*				
	Scatterer radius (mm)	0.56+				
	Relative permittivity of top layer	Effective permittivity of top layer (snow)				
	Relative permittivity of scatterer	1.0 , 0.0*				
	Background relative permittivity	3.26E+00	2.82E −01	3.16E+00	1.49E −02	
	Relative permittivity of bottom layer	5.88E+01	4.38E+01	5.90E+01	4.37E+01	
	Top surface RMS and correlation length	Same as bottom surface RMS and Correlation length of snow layer				
	Bottom surface RMS and correlation length (cm)	0.028 , 2.1+				
* and + denote averaged value and estimated value respectively						

	Ice Shelf Sites 2005					
	Parameters	Site W1		Site W2		Site W3
	Volume fraction of scatterer (%)	32*				
	Scatterer radius (mm)	1.1+				
	Relative permittivity of top layer	1.0 , 0.0				
	Relative permittivity of scatterer	1.65E+00	7.85E−05	1.75E+00	9.36E−05	1.58E+00	6.84E−05
	Background relative permittivity	1.0 , 0.0*				
	Relative permittivity of bottom layer	59.00 , 42.00*				
	Top surface RMS and correlation length (cm)	0.62	10.93	0.42	9.53	0.94	10.00
* and + denote averaged value and estimated value respectively						

APPENDIX C. TABLE 3: MODEL PARAMETERS FOR THEORETICAL PREDICTION

	Layer 1 (Snow)		Layer 2 (Sea Ice)	
Layer Thickness (m)	Mentioned in the text or graph			
Volume Fraction (%)	32%		2%	
Scatterer Radius (mm)	1.1*		0.56*	
Top Surface RMS height and correlation length (cm)	0.23E-02	5.50E-02	2.80E-04	2.10E-02
Bottom Surface RMS height and correlation length (cm)	2.80E-04	2.10E-02	2.80E-03*	2.10E-01*
	Real	Imaginary	Real	Imaginary
Effective relative permittivity of top layer	1.00	0.00	Effective relative permittivity of Layer 1	
Effective relative permittivity of scatterers	3.16	0.06	1.00 (Bubble)	0.00 (Bubble)
			40.08 (Brine)	42.57 (Brine)
Background relative permittivity	1.00	0.00	3.16	0.06
Effective relative permittivity of bottom layer	Effective relative permittivity of Layer 2		59.66	44.15
* Denotes estimated values based on [19].				

REFERENCES

1. Livingstone, C. E., P. S. Keshava, and A. L. Gray, "Seasonal and regional variations of active/passive microwave signature of sea ice," *IEEE Transactions on Geoscience and Remote Sensing*, Vol. 25, 159–173, 1982.
2. Shin, R. T., *Theoretical Models for Microwave Remote Sensing of Earth Terrain*, Ph.D. Dissertation, Department of Electrical Engineering and Computer Science, Massachusetts Institute of Technology, 1984.
3. Winebrenner, D. P., T. C. Grenfell, and L. Tsang, "On microwave sea ice signature modeling: Connecting models to the real world," *Proceedings in the IGARSS'92 Conference*, 1268–1270, Houston, 1992.
4. Fung, A. K., M. Dawson, and S. Tjuatja, "An analysis of scattering from thin saline ice layer," *Proceedings in IGARSS'92 Conference*, 1262–1264, Houston, 1992.

5. Fung, A. K., "Application of a combined rough surface and volume scattering theory to sea ice and snow backscatter," *IEEE Transactions on Geoscience and Remote Sensing*, Vol. 20, 528–536, 1982.
6. Golden, K. M., M. Cheney, K. H. Ding, A. K. Fung, T. C. Grenfell, D. Isaacson, J. A. Kong, S. V. Nghiem, J. Sylvester, and D. P. Winebrenner, "Forward electromagnetic scattering models for sea ice," *IEEE Transactions on Geoscience and Remote Sensing*, Vol. 36, No. 5, 1655–1674, 1998.
7. Lee, Y. J., W. K. Lim, and H. T. Ewe, "A study of an inversion model for sea ice thickness retrieval in ross island, antarctica," *Progress In Electromagnetics Research*, Vol. 111, 381–406, 2011.
8. Borgeaud, M., J. A. Kong, and F. C. Lin, "Microwave remote sensing of snow-covered sea ice," *Proceedings in IGARSS'86 Conference*, 73–89, Munich, 1986.
9. Borgeaud, M., S. V. Nghiem, R. T. Shin, and J. A. Kong, "Theoretical models for polarimetric microwave remote sensing of Earth terrain," *Journal of Electromagnetic Waves and Application*, Vol. 3, No. 1, 61–81, 1989.
10. Lin, F. C., J. A. Kong, and R. T. Shin, "Theoretical models for active and passive microwave remote sensing of snow-covered sea ice," *Proceedings in IGARSS'87 Conference*, 1121–1125, Michigan, 1987.
11. Lee, J. K. and J. A. Kong, "Active microwave remote sensing of an anisotropic random medium layer," *IEEE Transactions on Geoscience Remote Sensing*, Vol. 23, 910–923, 1985.
12. Lee, J. K. and J. A. Kong, "Passive microwave remote sensing of an anisotropic random medium layer," *IEEE Transactions on Geoscience Remote Sensing*, Vol. 23, 924–932, 1985.
13. Carlstrom, A., "A microwave backscattering model for deformed first-year sea ice and comparisons with SAR data," *IEEE Transactions on Geoscience and Remote Sensing*, Vol. 35, No. 2, 378–391, 1997.
14. Ulaby, F. T., R. K. Moore, and A. K. Fung, *Microwave Remote Sensing, Active and Passive, Vol. III: From Theory to Applications*, Artech House Inc., Norwood, 1986.
15. Tjuatja, S., A. K. Fung, J. Bredow, R. Hosseinmostafa, S. Gogineni, and V. Lytle, "Analysis of backscattering from snow covers on arctic and Antarctic sea ice," *Proceedings in IGARSS'93 Conference*, 1035–1037, Tokyo, 1993.
16. Ewe, H. T. and H. T. Chuah, "A study of dense medium effect

using a simple backscattering model," *Proceedings in IGARSS'97 Conference*, 1427–1429, Singapore, 1997.

17. Chuah, H. T., S. Tjuatja, A. K. Fung, and J. W. Bredow, "A phase matrix for a dense discrete random medium: Evaluation of volume scattering coefficient," *IEEE Transactions on Geoscience and Remote Sensing*, Vol. 34, No. 5, 1137–1143, 1996.
18. Fung, A. K., *Microwave Scattering and Emission Models and Their Applications*, Artech House, Norwood, 1994.
19. Chandrasekhar, S., *Radiative Transfer*, Dover, New York, 1960.
20. Fung, A. K. and H. J. Eom, "A study of backscattering and emission from closely packed inhomogeneous media," *IEEE Transactions on Geoscience and Remote Sensing*, Vol. 23, No. 5, 761–767, 1985.
21. Fung, A. K., Z. Li, and K. S. Chen, "Backscattering from a randomly rough dielectric surface," *IEEE Transactions on Geoscience and Remote Sensing*, Vol. 30, 356–369, 1992.
22. Ewe, H. T., H. T. Chuah, and A. K. Fung, "A backscatter model for a dense discrete medium: Analysis and numerical results," *Remote Sensing of Environment*, Vol. 65, No. 2, 195–203, 1998.
23. Albert, M. D., T. E. Tan, H. T. Ewe, and H. T. Chuah, "A theoretical and measurement study of sea ice and ice shelf in antarctica as electrically dense media," *Journal of Electromagnetic Waves and Applications*, Vol. 19, No. 14, 1973–1981, 2005.
24. Ewe, H. T., H. T. Chuah, and A. K. Fung, "A backscatter model for a dense discrete medium: Analysis and numerical results," *Remote Sensing of Environment*, Vol. 65, No. 2, 195–203, 1998.
25. Grenfell, T. C., "Surface-based passive microwave study of multiyear sea ice," *Journal of Geophysical Research*, Vol. 86, No. C9, 3485–3501, 1992.
26. Tjuatja, S., *Theoretical Scatter and Emission Models for Inhomogeneous Layers with Applications to Snow and Sea Ice*, Ph.D. Dissertation, University of Texas, Arlington, 1992.
27. Tjuatja, S., A. K. Fung, and J. Bredow, "A scattering model for snow-covered sea ice," *IEEE Transactions on Geoscience & Remote Sensing*, Vol. 30, No. 4, 804–810, 1992.
28. Ulaby, F. T., R. K. Moore, and A. K. Fung, *Microwave Remote Sensing, Active and Passive, Vol. II: Radar Remote Sensing and Surface Scattering and Emission Theory*, Addison-Wesley Publishing Company, Massachusetts, 1982.